RSC Advances

PAPER

View Article Online
View Journal | View Issue

Cite this: *RSC Adv.*, 2015, **5**, 20900

Porous ternary Fe-based catalysts for the oxidative dehydrogenation of ethylbenzene in the presence (absence) of carbon dioxide

Nuryana A. Ferreira,[a] Josué M. Filho[b] and Alcineia C. Oliveira*[a]

Received 15th November 2014
Accepted 3rd February 2015

DOI: 10.1039/c4ra14572k

www.rsc.org/advances

Porous ternary Fe-based catalysts were characterized and their catalytic properties through the oxidative dehydrogenation of ethylbenzene in the presence (ODH) or absence (DH) of carbon dioxide were investigated. The catalysts were characterized by X-ray diffraction (XRD), chemical analyses, thermoprogrammed reduction (TPR), physisorption measurements, Raman spectroscopy and scanning electron microscopy coupled to energy-dispersive X-ray spectrometry (SEM-EDX). The kinetic modeling of reverse water gas shift reaction (RWGS) and the effects of reaction parameters, such as reaction temperature and CO_2/H_2 ratio on the catalytic activity, were also investigated. The addition of Zn, La, Mg or Ni promoters to a porous Fe-based solid greatly enhanced the ODH reaction, whereas that of the RWGS is favoured by Ni promotion. The $CO_2/H_2 = 1$ ratio and temperature of 850 K were the best conditions for RWGS occurrence. The implications of these conditions on catalyst application for ODH and DH reactions were discussed. Ethylbenzene conversions were too low due to the decreased textural properties of some catalysts as well as the selectivity to styrene is inhibited. A porous FeAlZn catalyst exhibited higher catalytic performance than the other ternary solids in terms of the ethylbenzene dehydrogenation and resistance against deactivation, whereas low RGWS conversions were observed under the abovementioned conditions.

1. Introduction

The chemical recycling of carbon dioxide from combustion sources is a sustainable energy process because it allows for the strategy of capture and storage of CO_2 in reducing its emissions. In this sense, the use of CO_2 as a mild oxidant in catalytic reactions has been strongly encouraged. Moreover, alternative technologies for using carbon dioxide, such as wet partial oxidation or autothermal reforming, propane dehydrogenation, ethylbenzene dehydrogenation, and dry reforming, among others,[1–3] represent the further remarkable economic advantages of CO_2 consumption.

In additional, the growing concern about styrene production costs has directed the interests of researchers toward the development of the oxidative dehydrogenation of ethylbenzene in the presence of carbon dioxide (ODH). Styrene is a highly valuable monomer used for polymeric polystyrene resins and styrene–butadiene rubber production.[1–11] However, the commercial process of the direct-steam dehydrogenation of ethylbenzene (DH) to styrene leads to the use of a large amount of superheated steam.

Another limitation of the process is the low selectivity to styrene due to the formation of benzene and toluene as by-products, in addition to thermodynamic equilibrium limitations.[6–10] Thus, an ODH reaction in the presence of carbon dioxide offers advantages over a DH reaction, owing to CO_2 reducing the energy consumption, accelerating the reaction rate, prolonging catalyst lifetime, enhancing selectivity, and alleviating thermodynamic constraints; moreover, it could indeed drive the process towards green chemistry.[1–10]

The findings state that the DH reaction is coupled with reverse water gas shift (RWGS). Because the RWGS reaction is mildly endothermic with an enthalpy of 41.1 kJ mol^{-1}, the reaction is carried out at low temperatures. This makes the coupled process of an ODH reaction slightly endothermic, compared with that of DH.[9] Although the isolated RWGS reaction has no such difficulties, the catalytic stability is often poor. Thus, the solid is still not yet sufficiently developed for industrial application, although it has been widely investigated on a laboratory scale. In additional, RWGS reaction occurrence is undesirable for ethylbenzene dehydrogenation, dry reforming, and propane oxidation, among other reactions, due to the low yield of the products from these reactions.[5,12–14] Indeed, the kinetics of the RWGS reaction is studied at a low conversion and high hydrogen partial pressure and the reaction should be limited by dissociative CO_2 adsorption.

[a]*Universidade Federal do Ceará, Campus do Pici-Bloco 940, Fortaleza, Ceará, Brazil. E-mail: alcineia@ufc.br; Fax: +55 85 33 66 9982; Tel: +55 85 33 66 90 51*

[b]*Universidade Federal do Ceará, Departamento de Física, Fortaleza, Ceará, Brazil. Fax: +55 85 33 66 94 83; Tel: +55 85 3366 94 83*

The systematic exploitation of dehydrogenation of ethylbenzene coupled with RGWS would accomplish significant efficiency in styrene production and reduction in carbon dioxide emissions. A great deal of insight into the coupling reaction has been acquired by studying the catalytic activities of various solids based on iron oxides. Nanostructured Fe-containing promoters, such as alumina, zirconia or ceria, have shown good performance for catalyzing the oxidative dehydrogenation of ethylbenzene (EB) with CO_2. It is noteworthy to mention that the activity of *in situ* $FeAl_2O_4$ spinel-phase formation motivated us to investigate the catalytic properties of a FeAl solid by adding a third element in the catalyst composition.[10] As the stability of the $FeAl_2O_4$ phase in an ODH reaction is limited, owing to carbonaceous deposition, there is a need to develop new catalyst systems that allow for the uniform dispersion of the active phase, as well as high stability and driving the redox mechanism of the titled reaction to avoid an isolated occurrence of RGWS reaction. The addition of La, Mg, Zn or Ni in the Fe-based solids is expected to minimize the deactivation by phase transformation effects.

Thus, the aim of this study is to investigate the performance of nanostructured FeAlZn, FeAlLa and FeAlNi catalysts for styrene production. FeMgZn is used for comparison purposes. In addition, a deep comprehension of the DH and RWGS reaction conditions for improving the reaction yields or avoiding their occurrence is highly desirable, depending on the investigative focus. This study presents kinetic modeling and catalytic results for evaluating the effect of temperature and CO_2/H_2 ratio on the catalytic properties of Fe-based catalysts through RWGS and DH reactions. The investigations of the adsorption and deactivation constants, as well as the rate of the RWGS reaction in different temperatures, are also studied by the model.

2. Experimental

2.1. Catalyst preparation

The mixed oxides were prepared by the precipitation method using aluminum tri-sec-butoxide ($Al(OC_4H_9sec)_3$) and ferric nitrate $Fe(NO_3)_3 9H_2O$ as precursors.[10] In brief, aluminum tri-sec-butoxide was first dissolved into an excess of isopropanol and vigorously stirred at 333 K until the solution became homogeneous. Then, a mixture of 2.9 mol of water, ferric nitrate, and 6.5 mol of absolute ethanol together with lanthanum nitrate solution was added to the stirred mixture of aluminium through a peristaltic pump. The reactants were maintained under constant stirring and refluxing for 24 h. The gel was subsequently washed with ethanol, dried at room temperature and calcined at 873 K under air flow at a heating rate of 5 °C min^{-1} for 2 h. The abovementioned methodology was used to obtain the FeAlLa. Other solids, such as FeAlZn, FeAlNi and FeMgZn were also prepared, in which zinc, nickel and magnesium nitrate, were the active component precursors. The metal contents measured by chemical analyses were 60 : 20 : 20 mol%, respectively, for iron, aluminium and the third metal added to the solid.

2.2. Characterization

X-ray diffraction patterns (XRD) were measured on a PANalytical X'PERT HighScore X-ray diffraction equipment, under the following conditions: Cu target Kα radiation, scanning step of 0.02°, scanning rate of 0.1, and scanning current and voltage of 20 mA and 30 kV, respectively. The diffractograms were compared with those of JCPDS (Joint Committee on Powder Diffraction Standards).

Inductively Coupled Plasma Optic Emission Spectroscopy (ICP-OES) was performed with a Varian apparatus. Previously, the solids were digested with an equimolar mixture of nitric and hydrochloric acids at 90 °C in a sand bath. The actual metallic content of the solids was then determined by ICP-OES.

The adsorption–desorption isotherm experiments were carried out with an ASAP 2000 Micromeritics instrument to determine the specific surface areas and pore structure parameters of the solids. The probe molecule was nitrogen at 77 K in a surface area analyzer. Samples were degassed at 423 K for 12 h prior to measurement. The BET equation was used to calculate the total specific surface areas of fresh and spent catalysts. The pore distributions and surface areas of mesopores were calculated by the Barrett–Joyner–Halenda (BJH) method from the desorption branch of the isotherms.

The morphological aspects of the sample were determined by Scanning Electron Microscopy (SEM) measurements using an FEG Quanta 450 electron microscope equipped with an EDS Bruker QUANTAX system coupled to the SEM microscope, using an acceleration voltage of 2 kV.

Temperature programmed reduction (H_2-TPR) experiments were performed with homemade equipment using a quartz tube reactor possessing an inner diameter of 6 mm coupled to a thermal conductivity detector (TCD) for monitoring hydrogen consumption. The mass of the catalyst was 50 mg, and the experiment was carried out in the range of 323–1273 K. A mixture of 8% H_2/N_2 was used as a reducing gas with a rate of 100 mL min^{-1}, after passing through a 13× molecular sieve trap to remove water. Before the analysis, samples of *ca.* 0.1 g were placed in a tube reactor and heated under nitrogen at 373 K for 2 h.

The spent catalysts were characterized by Raman spectroscopy. The Raman measurements were obtained on a LabRam spectrometer (JobinYvon) under ambient conditions. A 532 nm argon ion laser was used as the exciting source on the sample surface with a power of 2 mW. Ten accumulated spectra were obtained in each spectral range, and the spectral resolution was 3 cm^{-1} in the 5–2000 cm^{-1} range. The Olympus lens focus was at 100 times magnification.

2.3. Catalytic testing

The dehydrogenation of ethylbenzene by CO_2 was carried out under steady-state conditions in a quartz fixed-bed reactor. The reactant mixture was composed of carbon dioxide and ethylbenzene at a 30 : 1 ratio. The flow rates used were N_2, 11.7 mmol h^{-1}; CO_2, 58 mmol h^{-1}; and EB, 1.98 mmol h^{-1} (CO_2/EB molar ratio of 30). The catalyst (50 mg) was crushed and activated *in situ* under a flow of nitrogen and was heated from room temperature to 823 K over the course of 1 h to

remove any gaseous impurities from the surface of the catalyst. The reaction was performed under atmospheric pressure at a temperature of 823 K, as previously defined by theoretical and experimental studies.[5] The product was analyzed by gas chromatography (GC) using a simple chrome chromatograph equipped with flame ionization detector (FID) and thermal conductivity detector (TCD). GC analyses were carried out at isothermal conditions from 295 to 523 K at a rate of 283 K min^{-1} and an injector temperature of 523 K.

The conversion and selectivity were defined in the following manner:

$$\%\text{EB conversion} = \frac{\text{EB}_{\text{in}} - \text{EB}_{\text{out}}}{\text{EB}_{\text{in}}} \times 100 \quad \text{(I)}$$

$$\%\text{EB selectivity} = \frac{\text{mol of desired product}}{\text{mol of reacted ethylbenzene}} \times 100 \quad \text{(II)}$$

Prior to the catalytic tests, modeling of DH[5] and RWGS reactions without the catalyst was performed to identify the best reaction conditions to perform the experimental analyses.

2.4. Model

The modeling of the experimental data is well suited to quantify the kinetic and thermodynamic effects of the RWGS reaction without using the catalysts. To include possible temperature, H_2/CO ratio and pressure effects on the Fe-catalyzed RWGS reaction, it is necessary to model the data. Thus, the thermodynamic–kinetic assessment was implemented and solved in the C^{++} program in the 400–1100 K temperature range. The reaction rates have been taken into consideration for defining the optimal conditions to operate the reaction.

2.4.1. Kinetic modeling. The kinetic model considers that the reverse water gas shift reaction (RWGS) is formally regarded as a single-step surface reaction (reaction (III)). CO_2 is assumed to be directly transformed into carbon monoxide and an oxygen radical by dissociative adsorption (reaction (IV)):

$$CO_2(g) + H_2(g) \rightleftharpoons CO(g) + H_2O(g), \quad \Delta H^{\circ}_{298.15\ \text{K}} = 41.17\ \text{kJ mol}^{-1} \quad \text{(III)}$$

$$CO_2(g) \rightleftharpoons CO(g) + O^{\bullet} \quad \text{(IV)}$$

Hence, the rate of carbon dioxide consumed, $-r'_{CO_2}$, is proportional to carbon monoxide produced, r'_{CO}, with reaction (IV) being the determining step of the reaction:

$$-r'_{CO_2} = r'_{CO} = k_{CO_2}\left(P_{CO_2}C_V - \frac{P_{CO}C_{OS}}{K_{CO}}\right) \quad (1)$$

where k_{CO_2} is the kinetic constant of velocity for CO_2, and P_{CO} is the partial pressure of CO. The ratio between the adsorption and desorption constants of CO is given as K_{CO}. In addition, it is assumed that the total amount of active sites occupied by oxygen atom and the number of active surface sites available per catalyst mass is equal to C_{OS} and C_v, respectively.

The first approach used for RGWS reaction assumes the fact that the adsorbed oxygen reacts with hydrogen from the gas phase, derived from the Eley–Rideal mechanism expression, as given below in reaction (V):[15]

$$H_2(g) + O^{\bullet} \rightleftharpoons H_2O(g) + {}^{\bullet} \quad \text{(V)}$$

Thus, the rate of water produced and consumed, r'_{H_2O}, is expressed in eqn (2):

$$r'_{H_2O} = k_{H_2O}\left(P_{H_2}C_V - \frac{P_{H_2O}C_V}{K_{H_2O}}\right) \quad (2)$$

In a second approach, the kinetics for the system under study adopts the steady-state condition for RWGS reaction, in which the rate of distinct and discreet site generation is zero and the following expression is presented for the rate of carbon dioxide:

$$-r'_{CO_2} = \frac{k_{CO_2}C_T\left(P_{CO_2} - \frac{P_{CO}P_{H_2O}}{P_{H_2}K_{CO_2}K_{H_2O}}\right)}{1 + \frac{P_{H_2O}}{P_{H_2}K_{H_2O}}} \quad (3)$$

Eqn (3) can be simplified by considering that k_{CO_2} is the ratio between adsorption and desorption constants because the former constant is much higher than the second constant, the expression is summarized as:

$$-r'_{CO_2} = k_{CO_2}P_{CO}C_T \quad (4)$$

2.4.2. Adsorption constants. Most simulation studies employ previously published adsorption constant expressions for similar catalysts in the RWGS reaction. The dependence of temperature on the adsorption of water and CO_2 constants can be calculated based on the following equations

$$K_{H_2O} = K^*_{H_2O}\exp\left[\frac{\Delta H_{H_2O}}{R}\left(\frac{1}{T} - \frac{1}{298.15}\right)\right] \quad (5)$$

$$K_{CO_2} = K^*_{CO_2}\exp\left[\frac{\Delta H_{CO_2}}{R}\left(\frac{1}{T} - \frac{1}{298.15}\right)\right] \quad (6)$$

where K_{H_2O} and K_{CO_2} are the adsorption of water and CO_2 constants, respectively; and $K^*_{H_2O}$ and $K^*_{CO_2}$ values are 3.52×10^{41} bar^{-1} and 1.24×10^{69} bar^{-1}, respectively. The enthalpy values for water and CO_2 at 298.5 K (ΔH_{H_2O} and ΔH_{CO_2}) are 393.5 kJ mol^{-1} and 393.8 kJ mol^{-1},[16] respectively.

The term used to quantify the attenuation of the velocity rate by of CO_2 and water adsorption on the catalyst surface, θ, is given in eqn (7)

$$\theta = \frac{1}{1 + K_{H_2O}f_{H_2O} + K_{CO_2}f_{CO_2}} \quad (7)$$

Accordingly, the term used to quantify the attenuation of the velocity rate by of CO_2 and water desorption on the catalyst surface, θ_d, is described in the following manner in eqn (8):

$$\theta_d = \frac{1}{1 + (K_{H_2O})_d f_{H_2O} + (K_{CO_2})_d f_{CO_2}} \quad (8)$$

where f_{H_2O} and f_{CO_2} represent the fugacity of water and CO_2, respectively. The values of $K^*_{H_2Od}$ and $K^*_{CO_2d}$ are 2.02×10^{-3} bar^{-1} and 9.89×10^{-3} bar^{-1}, respectively. The enthalpy values for water and CO_2 at 298.5 K (ΔH_{H_2Od} and ΔH_{CO_2d}) are 41.3 kJ mol^{-1} and 204.0 kJ mol^{-1}, respectively.[16–18] These values were also used to determine the terms that quantify both the water and CO_2 adsorption capacities during the deactivation of the catalyst, particularly K_{H_2Od} and K_{CO_2d}.

By summing up the reaction rates, the values of the kinetic constants for adsorption, θ, and desorption, θ_d, are determined in eqn (9) and (10).

$$k'_a = k_a\theta_a \quad (9)$$

$$k'_d = k_d\theta_d \quad (10)$$

It is important to note that k_a and k_d are previously determined by eqn (4) at 850 K, being 0.32 s^{-1} and 0.33 s^{-1}, respectively.

The velocity rate of RGWS is also predicted by varying the partial pressure of carbon dioxide and hydrogen to obtain optimal conditions for CO_2/H_2 trough reaction (III),[18] as shown in eqn (11).

$$r_{RGWS} = -322 \times 10^{-6}\, e^{\frac{-73600}{RT}} \frac{P}{T^3} p_{H_2} P_{CO_2} \quad (11)$$

2.4.3. Experimental results in RWGS. Experimental results in RWGS were carried out by using the most active solids. The Fe–Co-based catalyst, possessing a metal-to-iron ratio of 3 was synthesised according to a method previously reported[15] and calcined at 873 K under air flow. This catalyst was chosen due to its excellent structural and textural properties, which promoted the dry reforming of methane[19] and it showed to be a potential catalyst for RWGS.

The reverse water gas shift reaction was carried out in a microcatalytic system in a quartz tubular fixed-bed reactor. About 150 mg of catalysts were used with the reactor operating at various temperatures and a mixture of 5% CO_2/N_2 in a hydrogen atmosphere was introduced into the catalyst bed using a flow of 40 mL min^{-1}. The H_2/CO_2 molar ratio was 1 : 1, and the products of the reaction were analysed in a Varian chromatograph. Previously, the catalysts were *in situ* activated at 873 K under 5% H_2/N_2 for 1 h.

3. Results and discussion

3.1. Characterizations of the catalysts

3.1.1. XRD, textural properties and SEM-EDX. Fig. 1 shows the XRD patterns of the catalysts. All the XRD patterns possess relatively high intensity lines describing the crystalline character of the solids, except for FeAlLa. The latter exhibits diffuse diffraction peaks at 2θ = *ca.* 35°, which is attributed to the typical amorphous character of La_2O_3–Al_2O_3.[20] In additional, the characteristic diffractogram of FeAlLa could be attributed to La_2O_3 (JCPDS, 05-0602), $LaAlO_3$ (JCPDS 85-1071) or $LaAl_{12}O_{19}$ (JCPDS, 77-0335) phases or yet γ-Al_2O_3 (JCPDS, 10-04625). However, due to the broadness of the peaks, their presence is not determined. In addition, the reflections belonging to iron phases are not observed, which is probably due to their nanometric sizes or good dispersion in the La_2O_3–Al_2O_3 matrix. This feature is commonly found in materials prepared by the sol–gel and nanocasting methods.[21,22]

It is evident that FeAlZn has diffraction peaks assigned to γ-Fe_2O_3 (JCPDS 39-1346), ZnO (JCPDS, 89-0510) and γ-Al_2O_3 (JCPDS, 10-04625). Mixed-oxide phases such as $ZnAl_2O_4$ or $ZnFe_2O_4$, Fe_2O_3–Al_2O_3 could be formed, but calcination temperatures are too low to obtain these mixed oxides. The XRD pattern of FeMgZn displays MgO (JCPDS 18-1022), in addition to

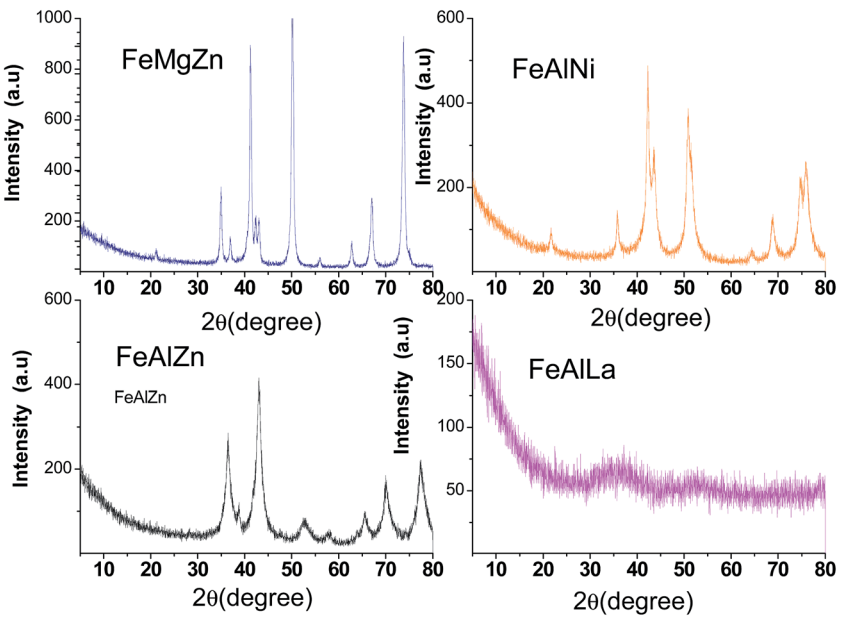

Fig. 1 XRD patterns of the fresh catalysts that were studied. The solids were calcined at 873 K under air.

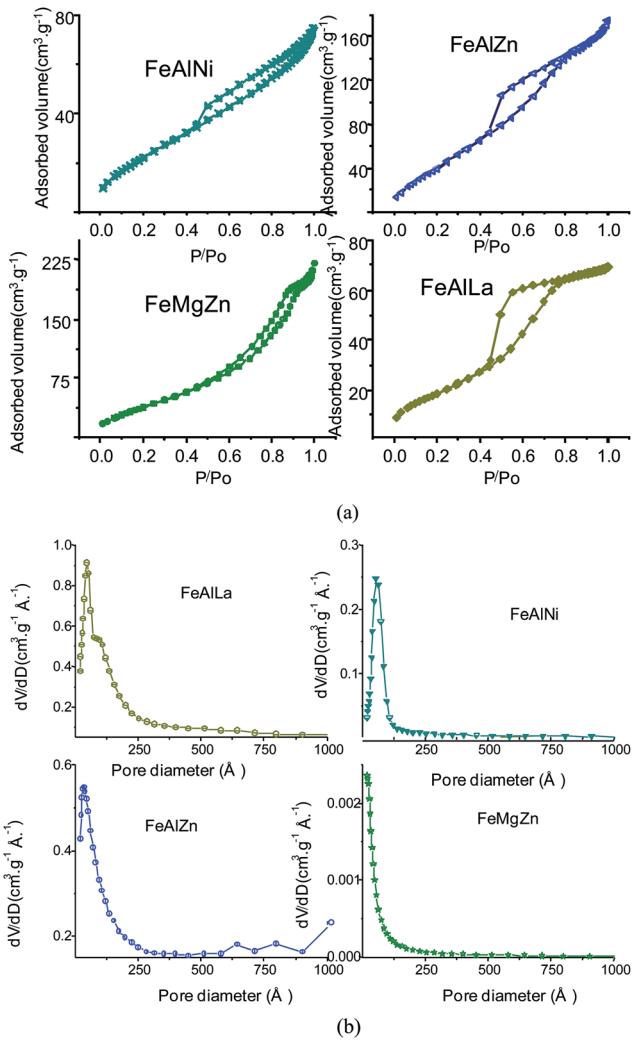

Fig. 2 (a) Nitrogen adsorption isotherms of the fresh catalysts. (b) The corresponding BJH pore-size distribution of the solids.

those of ZnO and γ-Fe_2O_3. The diffraction lines do not show any diffraction peak relative to $MgFe_2O_4$ due to the low heating temperature of the solid to generate this phase.[23] For FeAlNi, peaks ascribed to NiO (JCPDS 75-0197) and γ-Fe_2O_3 are visible, whereas those of α-Fe_2O_3 (JCPDS 79-1741) are obscurely observed. The reflections of $NiAl_2O_4$ and $FeAl_2O_4$ cannot be ruled out, and this implies that these generated spinel oxides compounds are highly dispersed over the bulk. Particle sizes estimated by the Scherrer equation show the nanosized features of the FeAlLa and FeAlZn, whereas the aggregation of FeMgZn and FeAlNi particles implies that the solids have large sizes.

The chemical analyses by ICP-OES results show that the obtained oxide composition is close to that predicted theoretically and corresponds to 68 wt% of Me_1, whereas 16 wt% for that of each Me_2 or Me_3 specie. If one considers all oxides having or $Me_1Me_2Me_3$ general formulae, the percentage of the elements matches well with the calculated values.

Nitrogen sorption isotherms show that FeAlLa, FeAlZn and FeAlNi catalysts have type IV isotherms with the hysteresis loop between H_2 and H_3 (Fig. 2), which is typical of mesoporous solids.

FeMgZn is an exception because its isotherm has a type II feature sorption curve. The specific surface area (Sg_{BET}) and pore volume (V_p) of FeAlLa are the largest among the oxides studied ($Sg_{BET} = 70\ m^2\ g^{-1}$; $V_p = 0.10\ cm^3\ g^{-1}$; $D_p = 39$ Å), as illustrated in Table 1. This might be due to their oxides being uniformly dispersed as nanocrystallites that are not observed by XRD. FeMgZn catalyst has a rather low surface area (*ca.* 46 $m^2\ g^{-1}$), and the other textural parameters, such as V_p of *ca.* 0.10 $cm^3\ g^{-1}$ and pore diameter of 11 Å, as well, indicate that this solid is microporous and possesses larger particle sizes. Furthermore, the pore diameters of FeAlZn and FeAlNi are reasonably large, and both Sg_{BET} and pore volumes slightly decreased.

The differences among the Sg_{BET} of the solids are not significant, rendering it a highly suitable surface area for solids obtained by the sol–gel method.[21,24] The particles sizes measured by XRD follows the same trends of the textural parameters values; moreover, the sintering effects during the calcination process could reduce the textural properties of FeAlNi and FeMgZn. This is in line with their particles sizes values of 21 and 44 nm, respectively, which are measured by XRD.

SEM-EDX images of the solids are illustrated in Fig. 3. The morphology of FeAlLa (Fig. 3a_1 and a_2) exhibits a platelet of LaAl-containing phases (*e.g.*, La_2O_3–Al_2O_3, La_2O_3 or $LaAlO_3$ or yet γ-Al_2O_3), in which the γ-Fe_2O_3 nanoparticles are mostly dispersed. This result indicates that FeAlLa appears to be composed of small particles of iron with size of *ca.* 2–20 nm, and the mean particle size of 30 nanoparticles is about 15 nm. This is further confirmed by EDX analysis that displays the uniform dispersion of iron nanoparticles on the La–Al surface

Table 1 Textural parameters obtained from the nitrogen adsorption–desorption isotherms. Sg_{BET} is the specific surface area calculated from the BET method in a relative pressure range of 0.05–0.2; V_p is the total volume calculated at a relative pressure of 0.99; D_p is the pore diameter at maximum of the pore-size distribution calculated by the BJH method from the adsorption branch. Ethylbenzene conversion and styrene selectivity were obtained using 50 mg of fresh catalyst at 823 K, CO_2/EB molar ratio of 30 for 5 h

Catalyst	L^a (nm)	Sg_{BET} ($m^2\ g^{-1}$)	V_p ($cm^3\ g^{-1}$)	$D_p{}^b$ (Å)	EB conversion^c (%)	Styrene selectivity^c (%)
FeAlNi	21	52	0.07	17	10	2
FeMgZn	44	46	0.06	11	6	100
FeAlZn	16	61	0.08	20	25	99
FeAlLa	—	70	0.10	39	17	95

[a] From the (311) reflection of γ-Fe_2O_3 observed by XRD. [b] From the desorption branch of the isotherms. [c] Steady-state condition.

(Fig. 3a), which is consistent with the XRD and textural properties results.

On the other hand, the morphology of FeAlNi is markedly different from other solids. Plate-like crystallites are clearly visible (Fig. $3b_1$ and b_2). The crystallites are believed to be composed of α-Fe_2O_3, γ-Fe_2O_3 and γ-Al_2O_3, as suggested by EDX analyses. The increased magnification to examine the plates shows that the homogeneously dispersed particles of NiO are on their surfaces. These results are in line with XRD measurements.

The SEM-EDX micrographs of FeAlZn reveals well-formed, thin plate-like crystals with sharp edges (Fig. $3c_1$ and c_2), which are indicative of α-Fe_2O_3 or γ-Fe_2O_3 and γ-Al_2O_3 presence. The existence of some of these phases is suggested by XRD. In additional, it is clearly observed that finely dispersed ZnO crystallites are superposed in the platelet at a size of *ca.* 100 nm, in line with XRD analysis. These features are associated with the elevated textural properties of the solid. In addition, a small amount of carbon from the aluminum precursor was found on the Al-containing samples.

From Fig. $3d_1$ and d_2, it can be observed that FeMgZn is formed by a small agglomeration of particles, which are superposed in a platelet. It consists of rather heterogeneous, large spherical-like particles with a mean size of 50 nm. These results are consistent with the crystallite size included in Table 1, which are obtained from XRD. They are also in agreement with the previous N_2 physisorption results that show the lowest textural properties for FeMgZn. Additional EDX analysis confirms the non-uniform distribution of MgO, ZnO and γ-Fe_2O_3 in some regions.

3.1.2. TPR analyses. TPR curves were obtained to determine the reducibility of the ternary oxide catalysts, as shown in Fig. 4.

The curves show two major peaks with maxima at low temperatures, centered at around 811 K, and a high-temperature reduction peak at 920 K, as for FeMgZn. It should be assumed that the TPR profiles of α-Fe_2O_3 and γ-Fe_2O_3 relate a first-reduction process of Fe^{3+} to Fe^{2+} at around 673 K, whereas a second peak at about 723 K is ascribed to the reduction of Fe^{2+} to metallic Fe.[9,21] Furthermore, pure ZnO and MgO do not reduce at temperatures as low as 1073 K.[25,26] As the temperatures of reduction take place at higher temperatures than those of the literature, the reduction of the iron species could be delayed due to a synergic interaction between iron, magnesium and zinc, favoring the redox properties of the material. Another possibility is the interaction between surface iron and MgO and ZnO species, forming other compounds in a reduction environment.[27] In addition, a third reduction peak up to 1073 K is suggested by TPR curve of FeMgZn. This curve could be attributed to the direct reduction of finely dispersed

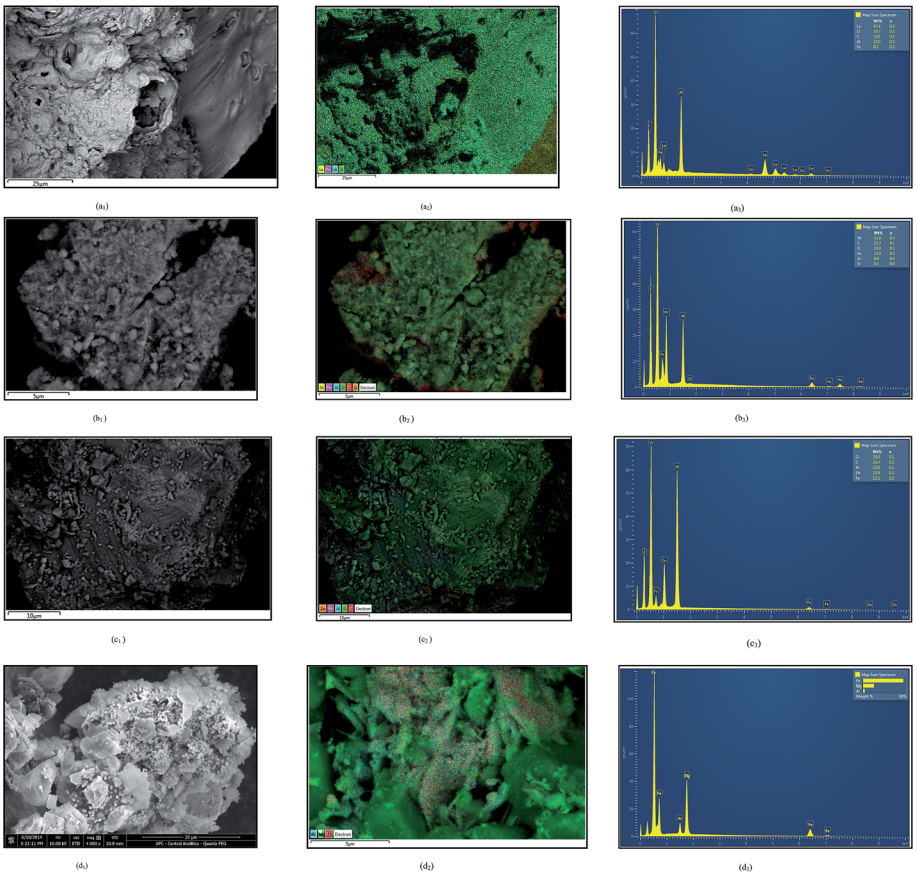

Fig. 3 SEM images of the fresh catalysts: FeAlLa (a_1 and a_2), FeAlNi (b_1 and b_2), FeAlZn (c_1 and c_2) and FeMgZn (d_1 and d_2). The EDX images are represented by a_3, b_3, c_3 and d_3 for FeAlLa, FeAlNi, FeAlZn and FeMgZn catalysts, respectively.

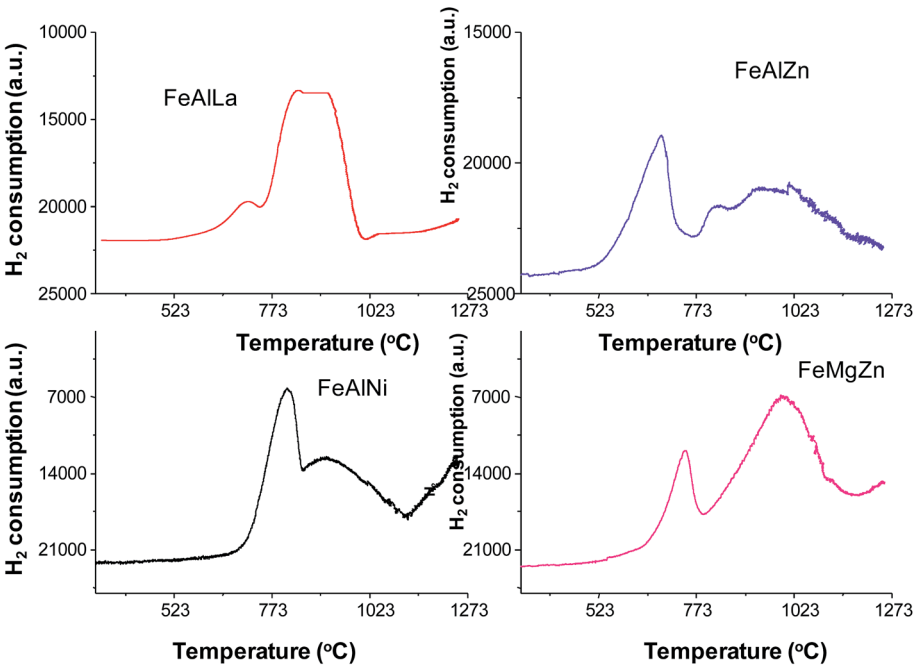

Fig. 4 TPR profiles of the fresh catalysts.

$MgFe_2O_4$ or $ZnFe_2O_4$ phases; these species show elevated temperatures of reduction on comparing with their bulk counterparts because they are strongly interacting with the support.[28,29]

Because γ-Al_2O_3, La_2O_3, $LaAlO_3$ or $LaAl_{12}O_{19}$ or even Al_2O_3–La_2O_3 phases do not exhibit reduction peaks at temperatures as low as 1273 K, the aforementioned reduction peaks of FeAlLa are associated to the finely dispersed iron-oxide reduction on the Al_2O_3 and/or La_2O_3 matrix. The latter enables the difficulty of iron-oxide reduction in the catalyst and thus decreases its degree of reduction, compared with FeMgZn.

The TPR profile of FeAlZn exhibits an asymmetric peak at *ca.* 680 K, which can attribute for the reduction of γ-Fe_2O_3 to Fe_3O_4. A broad peak in a much wider range from 440 to 943 K consists of two components with maxima at *ca.* 766 K and *ca.* 877 K and corresponds to the reduction of Fe^{2+} to Fe^0, respectively. With regard to this point, it should be emphasized that the reduction of magnetite to metallic iron is affected by the ZnO presence, probably due to FeO (wustite) formation,[9] whereas $FeAl_2O_4$ reduction does not occur in concomitance with that of other iron or zinc species.

The TPR profile of FeAlNi obviously displays that the reduction peaks of iron species shifts to the higher temperature and exhibits a remarkable broadening of the hydrogen uptake peak due to the formation of reduced metallic iron reduction over nickel aluminate or iron aluminate supports. According to the findings, both iron and nickel aluminate are formed by a solid-state reaction between γ-Al_2O_3 and iron or nickel counterparts under moderate temperatures and oxidative environments.[30–33] Typically, pure NiO is characterized by a single TPR peak at 573 and 673 K.[34–36] In addition, the peak position of water formation is not visible over all solids due to the detector limitation. Combining with the XRD results, the latter peak is not visible because it can be mainly dispersed in the solid matrix as nanoparticles.

3.2. Catalytic results in the dehydrogenation of ethylbenzene in the presence (absence) of CO_2

The catalytic performance is evaluated by the dehydrogenation of ethylbenzene to styrene over various catalysts. Blank runs provided almost negligible conversion after 5 h of reaction time in the absence of CO_2, whereas its presence gave 2% conversion.

Fig. 5a shows the overall conversion and selectivity obtained in 5 h of reaction time, when CO_2 is co-fed in the reaction.

The conversions are high (*e.g.*, up to 10%) in 1 h of reaction time over all solids. A possible reason for this performance is the cracking of ethylbenzene molecules due to the thermal effects at the beginning of the reaction.[9,21] The behavior of solids follows distinct trends as the reaction proceeds. FeAlNi retains 10% of the conversion along with the reaction time, whereas FeMgZn does not display significant catalytic activity in the same testing period, and its conversion gradually decreases with stabilization at 6% in the steady state (Table 1).

Judging from the fact that FeAlNi and FeMgZn possess the same active Fe^{3+}/Fe^{2+} sites from γ-Fe_2O_3 and that their textural properties (Table 1) are closer, the catalytic behavior can be rationally explained by the presence of their promoters. The findings[31,32] proposed a mixed acid–basic and reduction–oxidation mechanism for the reaction. There is a formation of π-adsorbed intermediate on Fe^{3+}, which is a Lewis acid center obtained from α-Fe_2O_3. This step is followed by the elimination of two hydrogen ions from two C–H ethylic groups on basic centers; the subsequent electron transfer to Fe^{3+} results in

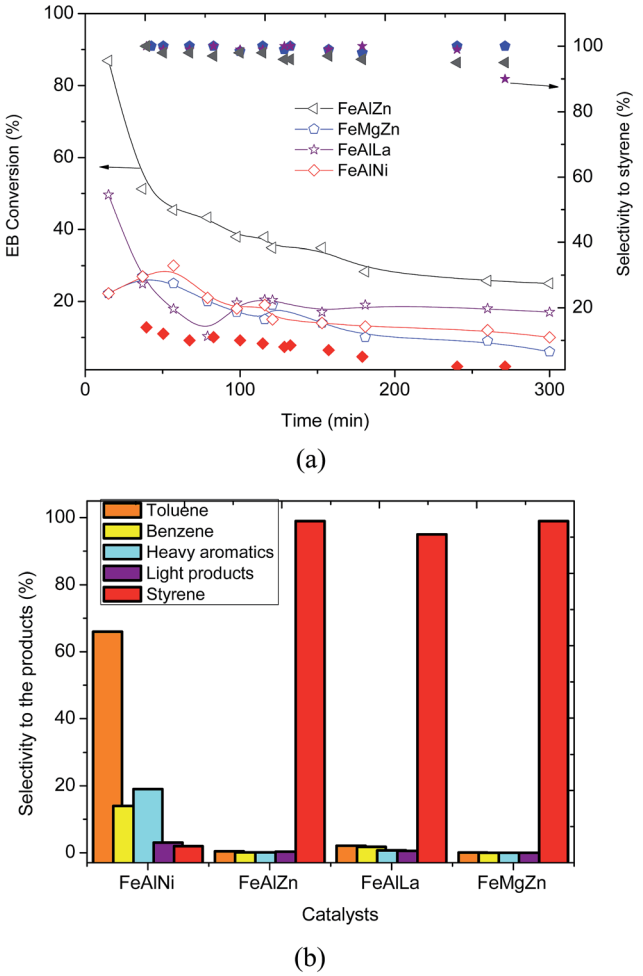

Fig. 5 (a) Catalytic results of the dehydrogenation of EB in the presence of CO_2. The open symbols represent the conversion, whereas the closed symbols are the selectivities to styrene. (b) Overall selectivity of the products formed during the reaction in 5 h. The reaction was performed under atmospheric pressure at 823 K and a CO_2/EB molar ratio of 30.

styrene and H_2 production. Bonfim *et al.* reported that[33] bulk Fe-containing ZnO oxides are seen as active phases for ethylbenzene conversion in the presence of steam because of the interaction between the acidic ZnO and α-Fe_2O_3, forming $ZnFe_2O_4$. Nevertheless, the activity decreases significantly with Zn^{2+} sites in the iron-based catalysts in the dehydrogenation of ethylbenzene in a He atmosphere[32] due to the easy reduction of the iron species. The same fact can probably be attributed to the deactivation behavior of FeAlZn.

However, using NiO as promoter, FeAlNi activity does not changed significantly, suggesting that the active Fe^{3+} is not sufficiently reducible, and the Fe^{3+}/Fe^{2+} reduction–oxidation couple is stabilized on the catalysts (shown by TPR), whereas Ni^{2+} is reduced to Ni^0, acting as active sites by increasing the occurrence of side reactions such as ethylbenzene cracking.[34,36] Moreover, the selectivity of styrene over FeMgZn reaches 99%, whereas the FeAlNi production of styrene is only 2% (Fig. 5b). By-products, such as toluene, benzene, aromatics, methane and other light products are also found over FeAlNi, indicating the predominance of ethylbenzene cracking and condensation reactions, as well as Boudouard reaction over Ni^0 sites.[34] For the purposes of comparison, a binary FeCo catalyst prepared by the co-precipitation method[35] is also used as a catalyst, obtaining *ca.* 5% of conversion and *ca.* 9% of styrene selectivity. According to our previous study,[36] both Co^0 and Ni^0 sites are indispensible elements for coking.

The catalytic reaction rate depends strongly on the dispersion degree of active components. FeAlZn and FeAlLa possess Fe^{3+} well dispersed in their large surfaces (XRD and textural properties), and the results depicted in Fig. 5 show that high conversions are achieved at relatively low reaction times (typically under 30 min). The conversions over the these solids decrease monotonically and a maximum of *ca.* 30% is observed for FeAlZn, whereas FeAlLa conversion is about 20% in 4 h of reaction time, with styrene being the main product. Nevertheless, the styrene selectivity is not entirely obtained over FeAlLa in 5 h and styrene conversion falls simultaneously to 17%. A rational reason for explaining the aforementioned results is that the dispersed nanoparticles expose terrace, corner and edge atoms, in addition to step atoms, as observed for Fe-based solids obtained by the same preparation method.[37] These types of defects may contribute to an increase of ethylbenzene adsorption on Fe^{3+}, whereas this action is not observed on La^{3+} or Al^{3+} sites. As the active species containing Fe^{3+} are consumed, conversion is decreased, and the parallel reaction of ethylbenzene conversion to benzene, ethylene and methane, among others, accounts for slightly low selectivity over FeAlLa, compared with FeAlZn.

Best results are achieved over FeAlZn because of the $FeAl_2O_4$ active-phase formation, which could be stabilized by ZnO as a textural and structural promoter of the iron species.[33] This catalyst exhibits better results in ODH reaction, compared with FeCo and FeNi, whose active phases are $CoFe_2O_4$ and $NiFe_2O_4$ spinel oxides, respectively.[34] The latter phases are not selective to styrene, and thus, stability is restricted to 2 h of reaction time. Another factor may be the occurrence of a parallel RGWS reaction increasing the CO_2 conversion at the expense of ethylbenzene dehydrogenation, in some cases. This was subsequently confirmed by the modeling and experimental assay of RWGS reaction studies with FeAlNi and FeCo catalysts.

It is important to note that CO_2 formed during the reaction on FeAlNi is sufficiently reactive to be converted on metallic Ni^o sites, whereas MgO adsorption ability for CO_2 is elevated rather than by other elements.[38] The reason for this behavior is believed to be due to the presence of either MgO or $MgAl_2O_4$ on FeMgZn, as previously stated. For FaAlZn, the ability of Zn sites in converting CO_2 can be quite low,[39] and thus, poor CO_2 conversion is expected. In the case of FeAlLa, lanthanum carbonates can be formed by the adsorption of CO_2,[40] and it can justify the catalytic performance of the solid.

As can be observed in Table 2, the catalytic performance is significantly affected in the absence of CO_2, *i.e.*, a DH reaction. The catalytic runs are performed far from equilibrium. When CO_2 is co-feeding the reaction, an enhancement of the EB conversion to 20% is obtained over FeAlNi, whereas the

conversion over FeMgZn is about 9% in 5 h of time on stream. The deactivation of FeAlNi observed in the ODH reaction (Fig. 5a) is probably due to the reduction of Ni particles by the products H_2 and CO in the RGWS reaction.

Catalytic performance in the absence of CO_2 (Table 2) displays twice as little as that of the parent solids used in the presence of the gas (Table 1). However, no general trend or correlation among iron dispersion, promoter nature and activity can be drawn from EB conversion data. From these results, it can be concluded that simple ethylbenzene dehydrogenation (DH reaction) occurrence is limited in the absence of the mild oxidant due to the reduction of the active iron phase. In addition, it appears that the styrene product is unstable in the absence of CO_2 and reacts with the loss of its selectivity. This will be further investigated over the most active solids.

3.2.1. Characterization of spent solids. The Raman measurements of the spent solids are performed to describe the structural features of the solids and confirm the existence of carbonaceous deposits after being tested in the reaction (Fig. 6).

FeAlLa exhibits two broad bands at around 1345 and 1620 cm^{-1}, which are attributed to the D and G bands, respectively; these bands are associated with the deposition of carbonaceous species on the solid surface. The D band is ascribed to the defects in the structure or disordered carbon species, whereas that of G is originated from the in-plane C–C bond stretching of more ordered graphitized carbon.[1] Most probably, some well-dispersed iron nanoparticles of FeAlLa are more prone to be reduced during the reaction, and thus, form metallic iron due to hydrogen presence. Assuming that coking formation is inevitable under the aforementioned conditions, the reason for a lower activity decay of the FeAlLa could be a higher resistance against a full reduction of the nanoparticles and leaching of the coking by oxi-lanthanum carbonate species formed by CO_2 from the solid surface.[41] More interestingly, Table 2 shows that the textural properties of spent FeAlLa are only slightly affected after the reaction, as compared with the fresh solid in Table 1.

In the case of FeAlNi, the shifting of D and G bands to higher wavenumbers is also observed, as compared with FeAlLa, particularly as the D band displays a 35 cm^{-1} red-shift. Raman results are in reasonable harmony with those aforementioned catalytic results that suggested the deactivation of this solid, owing to ethylbenzene cracking. This is in a good agreement with the report of Menezes[5] that illustrated the deactivation of

Table 2 Catalytic performance in the absence of CO_2 for the steady-state condition. Reaction conditions: 50 mg of fresh catalyst and a temperature of 823 K over the course of 5 h. The textural properties of the spent catalysts, after being used in the reaction in the aforementioned reaction conditions

Catalyst	EB conversion in the absence of CO_2 (%)	Sg_{BET} ($m^2\ g^{-1}$)	V_p ($cm^3\ g^{-1}$)
FeAlNi	20	19	0.03
FeMgZn	9	14	0.02
FeAlZn	2	54	0.07
FeAlLa	—	63	0.09

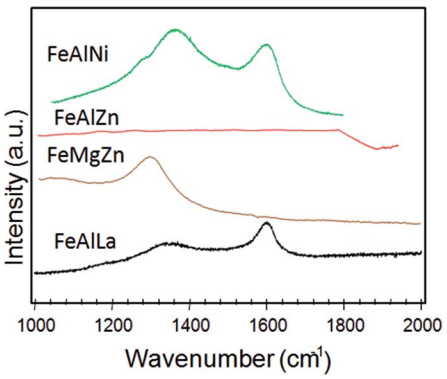

Fig. 6 Raman measurements for the spent catalysts. The solids were used in the reaction under atmospheric pressure at 823 K and a CO_2/EB molar ratio of 30 for 5 h.

Fe-based catalysts induced by metallic nickel species, which provides the cracking of the ethylbenzene molecule to form carbon on the solid surface. These results could not be explained without taking into account the damage of the solid surface. As shown in Table 2, the values of the textural properties of the solids decrease significantly, compared with the fresh solid, because of coking on the solid surface.

Investigating the Raman spectrum of FeMgZn more closely, it can be found in only one band, namely that of D. It implies that the amorphous carbon deposition from ethylbenzene or CO decomposition reactions could be responsible for the poor activity of the solid. A quite satisfactory relationship between Raman results and surface properties is evidenced in Table 2. The low textural properties of the FeMgZn can be ascribed to the much more amorphous carbon deposition on pores and/or solid surfaces.

No carbon bands are observed for FeAlZn, which is assumed to be due to resistance to the coking of the solid. This interpretation is reasonable if the textual properties are still maintained for the spent solid (Table 2). It can be assumed that FeAlZn is a stable catalyst for the reaction.

3.2.2. Kinetic constant and RWGS reaction rate determinations. Using the C^{++} programming tool, the effect of temperature on the RGWS reaction rate is performed with the CO_2/H_2 of 1 at 10 bar (Tables 3 and 4). Not surprisingly, at different operating temperatures (from 400 to 1050 K), the results show that the non-catalyzed reaction is favored by increasing the temperatures. However, temperatures higher than 850 K significantly slow k_{RWGS} due to the thermodynamic limitations of the process at elevated temperatures (Table 3). Therefore, side reactions such as CO dissociation into CO_2 and its further conversion to coking (reaction (VI)) prevails over the RGWS reaction at around 1100 K. Up to this temperature, the overall process becomes close to the maximum allowed by equilibrium, probably due to the equal velocity of WGS and RWGS reactions or CO_2 dissociation (VI).

$$2CO \rightleftharpoons CO_2 + \text{coke},\ \Delta H^{\circ}_{298.15\ K} = -172\ \text{kJ mol}^{-1} \qquad \text{(VI)}$$

From Arrhenius plots used to establish a good set of temperature-dependent rate parameters, a resultant activation

energy parameter of 4.01×10^3 J mol^{-1} is obtained in accordance with those found elsewhere.[42–45]

Thermodynamic parameters ΔG_r° and ΔH_r° are -3.2 kJ mol^{-1} and 42.3 kJ mol^{-1}, respectively, at 823 K. These values decrease with an increase in temperature, suggesting that the CO_2 hydrogenation is favored at high temperatures, otherwise the RGWS side reaction occurs inspite of the main reaction under these conditions. According to the DFT-refined microkinetic model studies and mechanistic predictions, the WGS reaction proceeds *via* a carboxyl (COOH) mechanism, whereas the RGWS reaction proceeds according to that of a redox (reaction (IV)) at moderate temperatures,[42,45] which is in good agreement with our results.

3.2.3. Adsorption and desorption constants by varying the temperature. The CO_2 and water adsorption constants (*e.g.*, K_{CO_2} and K_{H_2O}) are obtained by the means of eqn (5) and (6). The plots of predicted adsorption constants as a function of temperature are shown in Fig. 7.

Because of the slight endothermicity of the RWGS reaction, K_{CO_2} gradually increases with increasing temperature (Fig. 7a). In addition, elevated temperatures lead to higher K_{CO_2} values than those of K_{H_2O}, and this is also reflected in their velocity rates. These differences are appreciable at temperatures less than 950 K, in which RWGS is thermodynamically favored.[43] Many mathematical models have been developed by investigators to predict the evolution of the effective RGWS reaction on a solid surface and mostly agreed that CO_2 adsorption is favored at temperatures lower than 850 K, due to mono and bidentate compound formation with CO_2, on the catalyst surface.[44]

It has been assumed that when temperatures are higher than 950 K, the parameter tends to reflect values close to zero because of the difficulty in adsorbing CO_2 on the solid surface. Thus, the CO_2 more rapidly decomposes to carbon monoxide and the traces of the effluents are detected in low amounts, resulting in reduced desorption constants.

The influence of the reaction temperature on the K_{H_2O} behavior is examined in temperatures ranging from 850 to 1000 K (Fig. 7b). The model considering water adsorption gives reasonable results, and the main reason is the good capture of water at temperatures as low as 950 K. Furthermore, the curves provide reasonable accuracy and good agreement with the fact that RWGS reaction is favored upon using these conditions, as

Table 3 Number of assays (NPt), temperature (T) and velocity constant (k_{RGWS}) values for RWGS reactions. The results were obtained from 400 to 1050 K by using a CO_2/H_2 molar ratio of 1

NPt	T (K)	$k_{RGWS} \times 10^2$ (s^{-1})
1	400	0.07
2	450	0.3
3	500	0.8
4	550	2.0
5	600	4.0
6	650	7.0
7	700	11.0
8	750	18.0
9	800	26.0
10	850	32.0
11	900	33.0
12	950	35.0
13	1000	36.0
14	1050	37.0

Table 4 Number of assays (NPt), carbon dioxide to hydrogen partial pressure (p_{CO_2}/p_{H_2}) and RWGS reaction rates

NPt	p_{CO_2}/p_{H_2}	$r_{RGWS} \times 10^{19}$ (kmol kg^{-1})
1	0.5	0.39
2	1	1.57
3	2	3.14
4	3	4.71
5	4	6.29
6	5	7.86
7	6	9.43
8	7	11.01
9	8	12.58
10	9	14.15
11	10	15.72

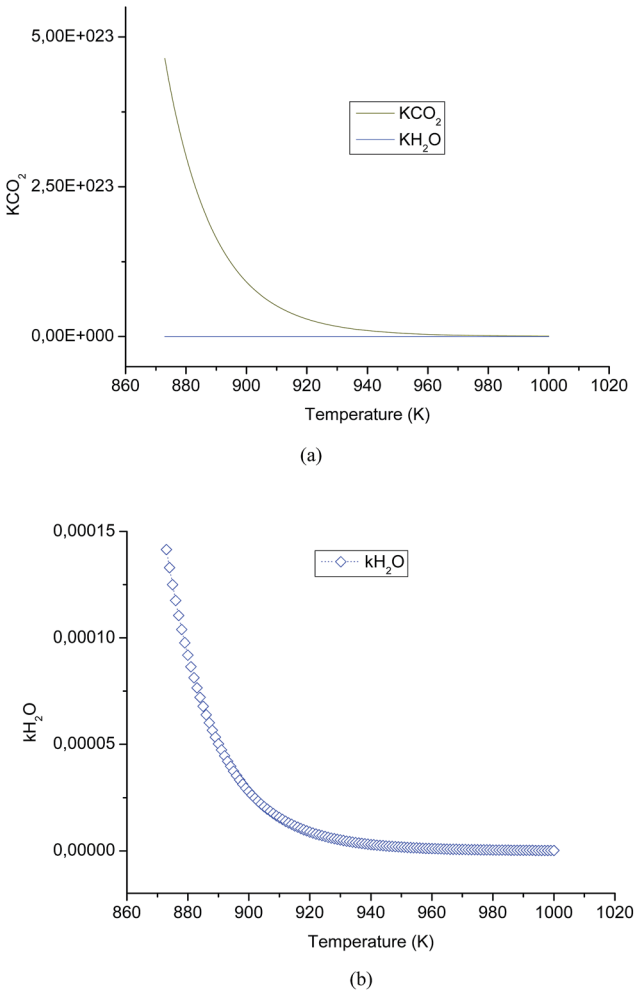

Fig. 7 (a) CO_2 adsorption constant at various temperatures obtained for a hypothetic catalyst surface. (b) Water adsorption constant as a function of the temperature for the aforementioned hypothetical catalyst surface.

observed for catalytic runs over Ru and carried out at 850 K.[47] It is interesting to consider the aforementioned observations in light of the recently reported Cu–Fe catalysts tested under the same conditions, which demonstrate the abilities of CO and water to desorb from Cu–Fe surfaces during the steam reformation of methane.[19]

Fig. 8 displays the plots of deactivation constants (*e.g.*, K_{H_2Od} and K_{CO_2d}) *versus* temperature.

Of all the models considering a hypothetic surface where CO and H_2O species react,[39,42,48] the curve provides the best fit to corroborate that the deactivation of these entities on a solid surface is faster over CO_2 than H_2O at temperatures as low as 950 K. This result indicates that the reaction is more favorable at temperatures lower than 950 K, as the reactant molecules of CO_2 disproportionate to form CO, and the rate of this reaction is too high, compared with other parallel reactions.[42,48]

The value of adsorption constant (k'_a) is found to be equal to 7.9×10^{-25} s^{-1} at 850 K by using eqn (7). The reaction in this study is more influenced by an increase in the reaction temperature. In addition, the deactivation on the external surface of the catalyst is assisted by a CO_2 decomposition parallel reaction more than its own CO_2 adsorption. Finally, the plots of adsorption constants *vs.* temperature result in an exponential curve, which is regarded as sufficiently good to indicate that temperatures below 950 K are adequate to show that the CO_2 adsorption rate is the determining step of the reaction, which is sufficiently elevated to allow for RWGS parallel reactions. However, the CO_2 deactivation rate is also enhanced at these temperature conditions. In addition, the model shows a strong tendency to underestimate the conversions at elevated temperatures.

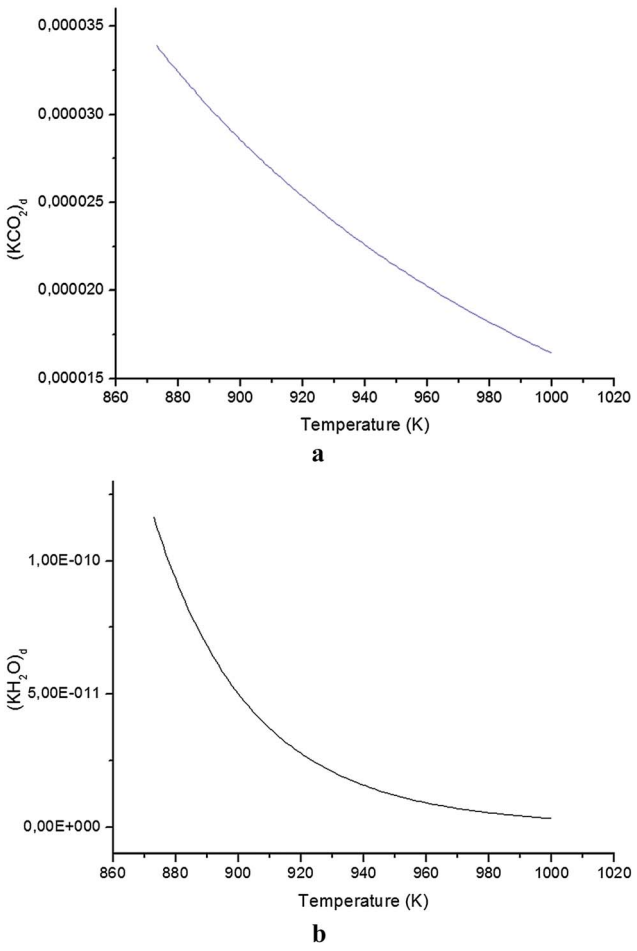

Fig. 8 (a) Deactivation constants of CO_2 obtained for a hypothetic catalyst. (b) Deactivation constants of water for a hypothetic catalyst.

3.2.4. Effect of CO_2/H_2 on the occurrence of RWGS. The reverse water gas shift reaction is studied under distinct CO_2/H_2 ratios by varying the temperature. RWGS reaction rates is gradually enhanced by increasing the partial pressure of the reactants (Table 4) due to the shift of equilibrium to form CO and water, as it has already been stressed in the literature.[49,50]

Lower CO_2/H_2 inferior to 1 corresponds to an increase in H_2 content in the feed and this can favor the competition among the following reactions: WGS (backward reaction (III)), hydrogenation of CO_2 to methanol or ethanol (reactions (VII–IX)), methane formation (reaction (X)), alkenes formation (reactions (XI and XII)) and coking by CO reduction (reaction (XIII)).[25,26] Moreover, RWGS is not thermodynamically favored under lower CO_2/H_2, indicating that the kinetic factors prevail over the thermodynamic ones.

$$CO_2 + 3H_2 \rightarrow CH_3OH + H_2O \quad \text{(VII)}$$

$$CO_2 + 4H_2 \rightarrow CH_3OH + 2H_2O \quad \text{(VIII)}$$

$$2CO_2 + 6H_2 \rightarrow C_2H_5OH + 3H_2O \quad \text{(IX)}$$

$$CO_2 + 4H_2 \rightarrow CH_4 + 2H_2O \quad \text{(X)}$$

$$2CO_2 + 7H_2 \rightarrow C_2H_6 + 4H_2O \quad \text{(XI)}$$

$$3CO_2 + 9H_2 \rightarrow C_3H_6 + 6H_2O \quad \text{(XII)}$$

$$CO_2 + 2H_2 \rightarrow C + 2H_2O \quad \text{(XIII)}$$

Nevertheless, the rates reach a plateau and a maximum value of $CO_2/H_2 = 1$, which tends to be favored due to the stoichiometric relations of the RGWS reaction even if elevated conditions are obtained at CO_2/H_2 ratios superior to 1. Therefore, reaction rate levels up 1.0×10^{-19} mol h^{-1} are achieved at p_{CO_2}/p_{H_2} reaching 1.

Apart from the modeling results, RWGS reaction occurrence is preferred at a CO_2/H_2 molar ratio of 1 and a temperature of 850 K.

3.3. Experimental studies in RWGS over the catalysts studied

Catalytic runs in the RGWS reaction were carried out over FeAlNi and FeCo (Fig. 9), the latter being a reference catalyst. The reaction conditions are the CO_2/H_2 molar ratio of 1 and a temperature of 850 K. A detailed description of FeCo reference catalyst and its textural and structural features of the solids have been given in ref. 42. The FeMgZn and FeAlLa catalysts are not active in the RGWS reaction due to the lack of active sites to

catalyze the reaction, whereas the conversion of FeAlZn shows activity in the first minutes of the reaction and then falls to zero.

Experimental and both experimental and predicted conversion have shown good fit.

The CO_2 conversion of Fe-based catalysts increases rapidly from 0 to 2.5% at 600 K, and thereafter, it appears that best catalytic activity can be attained with 20.3% conversion at 1400 K (Fig. 9a). Both the CO_2 conversion and CO selectivity do not follow the same trends due to WGS reaction predominance over certain catalysts, as shown in Fig. 9b. Instead, FeAlZn is inactive even at high temperatures. It is well known that Ni in iron-based catalysts promotes the WGS reaction at temperatures as high as 600 K due to reaction kinetic control, and the catalyst is very active, stable and selective to CO at high temperatures.[49–52] The FeAlNi is activated more rapidly; however, after 1 h of reaction, it quickly got deactivated mainly due to the formation of coke residues on the catalysts during the test. Carbon monoxide selectivity linearly decreases with an increase in temperature, ensuring that the catalytic activity for CO decomposition to coking at elevated temperatures is likely. This is favored when reduced nickel particles are present on the surface of the support.

Moreover, the inverse relationship between CO selectivity and temperature also suggests that the RWGS endothermic reaction needs heat to achieve high CO_2 conversion. Because extremely high temperatures are impractical for the commercial application of catalysts in the RWGS reaction, thermodynamically favorable parallel reactions, such as Boudouard (reaction (X)) and methanation (reaction (XIII)), could be likely over the FeAlNi catalyst. In the case of FeAlZn, the oxidation of iron nanoparticles may not be likely; as a result, there is a loss of the active sites needed for the reaction, and thus, CO selectivity is meaningless in the range of temperatures studied. The results indicated that the metallic Co nanoparticles are mainly responsible for the catalytic performance because the FeCo shows two times higher activity than the FeAlNi catalyst. Such an observation hints towards how the reaction conditions (temperature and composition) can affect the catalytic conversion. The results are indeed in excellent agreement with those obtained theoretically.

From these results, it can be concluded that FeAlZn is very advantageous in ethylbenzene conversion in the presence of CO_2 for producing styrene because the coupled reaction and the stability of the dispersed iron-active phase makes the occurrence of RGWS reaction effectively reduced.

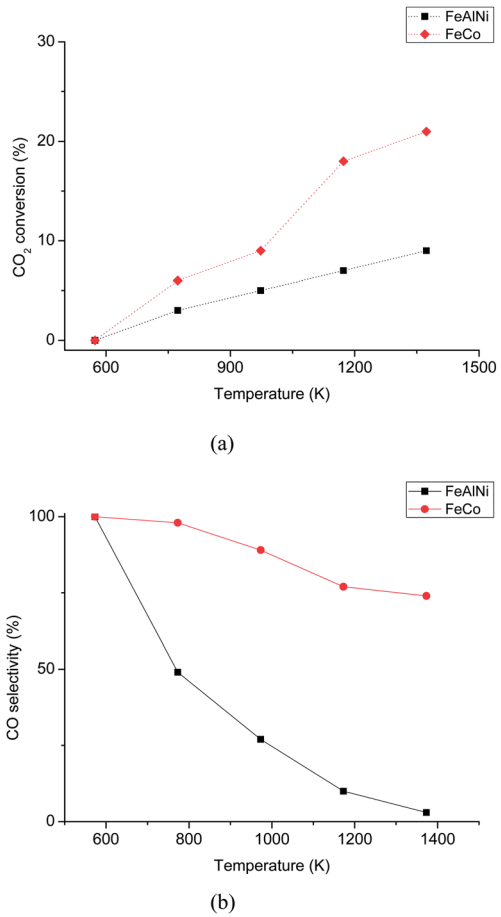

Fig. 9 Experimental assays of RWGS reactions for FeAlNi and FeCo catalysts: (a) CO_2 conversion and (b) selectivity to CO.

4. Conclusions

The ethylbenzene dehydrogenation in the presence of CO_2 (or its absence) was investigated over Fe-based catalysts. Among the various studied ternary systems that contained La and Zn promoters, FeAlZn showed the best results in ODH due to the dispersion of α-Fe_2O_3 and γ-Fe_2O_3 nanoparticles on their matrices in the presence or absence of CO_2. FeAlZn was the most active solid in the ODH reaction, whereas FeAlNi exhibited the best performance in the DH reaction among the catalysts studied. Catalytic results in the RWGS reaction were performed by the means of kinetic modeling and experimental studies. The optimal conditions for RWGS reaction occurrence were at 850 K, using a ratio of $CO_2/H_2 = 1$, which were proved by the experimental results for FeAlNi. The CO_2 adsorption constant decreased with an increase in temperature; this factor was responsible for the highest reaction rate at temperatures close to 850 K, due to CO_2 disproportionate reaction occurrences. Although the reaction rate was elevated at high hydrogen and carbon dioxide partial pressures, the CO_2/H_2 ratio values less than 1 led to the formation of hydrocarbons, whereas those superior to the unity gave CO_2 degradation. A $CO_2/H_2 = 1$ ratio and temperature of 850 K were the best condition for RWGS reaction occurrence, whereas that of the ODH was not favoured under these conditions. From the catalytic results, the FeAlZn showed a poor performance in RGWS reaction, compared with that of the FeAlNi catalyst due to the active-phase degradation of the former solid. Thus, FeAlZn is best suited for ethylbenzene dehydrogenation coupled to RGWS, and this solid exhibited 30% of ethylbenzene conversion, being entirely selective to styrene.

Abbreviations

C_{OS}	Active sites occupied by oxygen atom
C_T	Total amount of active sites occupied

C_v	Active surface sites available per catalyst mass
ΔH_{CO_2}	CO_2 enthalpy, kJ mol^{-1}
ΔH_{H_2O}	Water enthalpy, kJ mol^{-1}
f_{CO_2}	Fugacity of CO_2, bar
f_{H_2O}	Fugacity of H_2O, bar
K_{CO}	Ratio between the adsorption and desorption constants of CO
K_{CO_2}	Ratio between the adsorption and desorption constants of CO_2
K_{H_2O}	Ratio between the adsorption and desorption constants of H_2O
$K^*_{H_2O}$	Capacity for H_2O adsorption at reference temperature (548 K), bar^{-1}
$K^*_{CO_2}$	Capacity for CO_2 adsorption at reference temperature (548 K), bar^{-1}
k'_a	Kinetics constant for adsorption (eqn (9))
k'_d	Kinetics constant for desorption (eqn (10))
k_a	Kinetic constant for adsorption without products influence, s^{-1}
k_d	Kinetic constant for desorption without products influence, s^{-1}
K_{H_2O}	Kinetic constant of velocity for H_2O
k_{CO_2}	Kinetic constant of velocity for CO_2
P_{CO}	Partial pressure of CO, bar
P_{CO_2}	Partial pressure of CO_2, bar
P_{H_2}	Partial pressure of H_2, bar
P_{H_2O}	Partial pressure of H_2O, bar
$-r'_{CO_2}$	Rate of carbon dioxide consumed (eqn (1))
r'_{H_2O}	Rate of water produced (eqn (2))
r_{RWGS}	Velocity rate of RWGS (eqn (11))
θ	Attenuation of the velocity rate by CO_2 and water adsorption (eqn (7))
θ_d	Attenuation of the velocity rate by CO_2 and water desorption (eqn (8))

Acknowledgements

We gratefully acknowledge FUNCAP (0011-00206.01.00/09) and CNPq (473568/2012-8) for the financial support. The authors are also acknowledged to Central Analítica da UFC for SEM-EDX analyses.

References

1 A. L. Pinheiro, A. N. Pinheiro, A. Valentini, J. M. Filho, F. F. D. Sousa, J. R. Sousa, M. G. C. Rocha, P. Bargiela and A. C. Oliveira, *Catal. Commun.*, 2009, **11**, 11–14.
2 J. Li, C. Hu, K. Tong, H. Xiang, Z. Zhu and Z. Hu, *RSC Adv.*, 2014, **4**, 44377–44385.
3 N. R. Shiju, M. Anilkumar, S. P. Gokhale, B. S. Rao and C. V. V. Satyanarayana, *Catal. Sci. Technol.*, 2011, **1**, 1262–1270.
4 C. Nederlof, V. Zarubina, I. V. Melián-Cabrera, E. H. J. Heeres and F. Kapteijn, *Appl. Catal., A*, 2014, **476**, 204–214.
5 I. M. Nogueira, G. Q. Sabadia, A. A. Moreira, J. M. Filho and A. C. Oliveira, *J. Mol. Catal. A: Chem.*, 2011, **351**, 81–92.
6 X. Ye, Y. Yue, C. Miao, Z. Xie, W. Hua and Z. Gao, *Green Chem.*, 2005, **7**, 524–528.
7 C. L. Lima, O. S. Campos, A. C. Oliveira, F. F. de Sousa, J. M. Filho, P. L. Neto, A. N. Correia, G. Q. Sabadia, I. M. Nogueira, G. S. Pinheiro and A. C. Oliveira, *Appl. Catal., A*, 2011, **395**, 53–63.
8 S. Zhang, X. Li, J. Jing, H. Fan, Q. Wang and W. Li, *Catal. Commun.*, 2013, **34**, 5–10.
9 J. C. S. Araujo, F. N. A. Freire, C. B. A. Souza, A. C. Oliveira, A. P. Ayala and A. C. Oliveira, *Appl. Catal., A*, 2010, **377**, 55–63.
10 A. J. R. Castro, J. M. Soares, J. M. Filho, A. C. Oliveira, A. Campos and E. R. C. Milet, *Fuel*, 2013, **108**, 740–748.
11 Q. Wang, X. Li, W. Li and J. Feng, *Catal. Commun.*, 2014, **50**, 21–24.
12 A. Aouissi, D. Aldhayan and S. Alkathani, *Chin. J. Catal.*, 2012, **33**, 1474–1479.
13 F. F. de Sousa, H. S. A. de Sousa, A. C. Oliveira, M. C. C. Junior, A. P. Ayala, E. B. Barros, B. C. Viana, J. M. Filho and A. C. Oliveira, *Int. J. Hydrogen Energy*, 2012, **37**, 3201–3212.
14 V. Zarubina, C. Nederlof, B. van der Linden, F. Kapteijn, H. J. Heeres, M. Makkee and I. Melián-Cabrera, *J. Mol. Catal. A: Chem.*, 2014, **381**, 179–187.
15 S. Patel and K. K. Pant, *Chem. Eng. Sci.*, 2007, **62**, 5425–5435.
16 W. M. Haynes, *CRC, Handbook of Chemistry and Physics*, National Institute of Standards and Technology, Boulder, Colorado, USA, 3rd edn, 2012.
17 J. Erena, I. Sierra, A. T. Aguayo, A. Ateka, M. Olazar and J. Bilbao, *Chem. Eng. J.*, 2011, **174**, 660–667.
18 C. Hermann, E. Quicker and R. Dittmeyer, *J. Membr. Sci.*, 1997, **136**, 161–172.
19 D. C. Carvalho, N. A. Ferreira, J. M. Filho, A. C. Oliveira, O. P. Ferreira and J. M. Soares, *Catal. Today*, 2014, DOI: 10.1016/j.cattod.2014.08.010, in press.
20 M. Benito, S. Garcıa, P. Ferreira-Aparicio, L. G Serrano and L. Daza, *J. Power Sources*, 2007, **169**, 177–183.
21 A. J. R. Castro, S. P. D. Marques, J. M. Soares, J. M. Filho, G. D. Saraiva and A. C. Oliveira, *Chem. Eng. J.*, 2012, **209**, 345–355.
22 A. Barrera, M. Viniegra, V. H. Lara and P. Bosch-Giral, *Catal. Commun.*, 2004, **5**, 569–574.
23 G. A. El-Shobaky and A. A. Mostafa, *Thermochim. Acta*, 2003, **408**, 75–84.
24 Y. Lee, K. Jun, J. Park, H. S. Potdar and R. C. Chikate, *J. Ind. Eng. Chem.*, 2008, **14**, 38.
25 W. Jianxin and L. Laitao, *Catal. Lett.*, 2008, **126**, 325–332.
26 F. Mirzaei, M. Rezaei, F. Meshkani and Z. Fattah, *J. Ind. Eng. Chem.*, 2015, **21**, 662–667.
27 A. E. Palomares, A. Uzcátegui and A. Corma, *Catal. Today*, 2008, **137**, 261–266.
28 R. J. Balasamya, B. B. Topea, A. Khurshida, A. A. S. Al-Alia, L. A. Atanda, K. Sagata, M. Asamoto, H. Yahirob, K. Nomurac, T. Sanod, K. Takehiraa and S. S. Al-Khattaf, *Appl. Catal., A*, 2011, **398**, 113–122.
29 L. Ma, R. Wua, H. Liua, W. Xua, L. Chenb and S. Chen, *Solid State Sci.*, 2011, **13**, 2172–2176.

30 P. H. Bolt, F. H. P. M. Habraken and J. W. Geus, *J. Solid State Chem.*, 1998, **135**, 59–69.
31 N. Dulamiţă, A. Măicăneanu, D. C. Sayle, M. Stanca, R. Crăciun, M. Olea, C. Afloroaei and A. Fodor, *Appl. Catal., A*, 2005, **287**, 9–18.
32 P. Kuśtrowski, L. Chmielarz, A. Rafalska-Łasocha, B. Dudek, A. Pattek-Janczyk and R. Dziembaj, *Catal. Commun.*, 2006, **7**, 1047–1052.
33 H. E. L. Bonfim, A. C. Oliveira and M. C. Rangel, *React. Kinet. Catal. Lett.*, 2003, **80**, 359–364.
34 R. M. Freire, F. F. de Sousa, A. L. Pinheiro, E. Longhinotti, J. M. Filho, A. C. Oliveira, P. C. Freire, A. P. Ayala and A. C. Oliveira, *Appl. Catal., A*, 2009, **359**, 165–179.
35 D. C. Carvalho, N. A. Ferreira, J. M. Filho, A. C. Oliveira and O. P. Ferreira, Dry reforming of methane over mixed oxides obtained from thermal decomposition of layered double hydroxides, in *XXII International Materials Research Congress*, 2013, p. 60.
36 A. H. M. Batista, F. F. Sousa, S. B. Honorato, A. P. Ayala, J. M. Filho, F. W. Sousa, A. N. Pinheiro, J. C. S. Araujo, R. F. Nascimento, A. Valentini and A. C. Oliveira, *J. Mol. Catal. A: Chem.*, 2010, **315**, 86–98.
37 R. A. Van Santen, *Acc. Chem. Res.*, 2008, **42**, 57–66.
38 J. Feng, Y. Ding, Y. Guo, X. Li and W. Li, *Fuel*, 2013, **109**, 110–115.
39 F. Arena, G. Italiano, K. Barbera, S. Bordiga, G. Bonura, L. Spadaro and F. Frusteri, *Appl. Catal., A*, 2008, **350**, 16–23.
40 D. C. Carvalho, H. S. A. de Souza, J. M. Filho, A. C. Oliveira, A. Campos, E. R. C. Milet, F. F. de Sousa, E. Padron-Hernandez and A. C. Oliveira, *Appl. Catal., A*, 2014, **473**, 132–145.
41 H. S. A. de Sousa, A. N. da Silva, A. J. R. Castro, A. Campos, J. M. Filho and A. C. Oliveira, *Int. J. Hydrogen Energy*, 2012, **37**, 12281–12291.
42 M. J. L. Gines, A. J. Marchi and C. R. Apesteguia, *Appl. Catal., A*, 1997, **154**, 155–171.
43 S. P. Naika, T. Ryub, V. Buib, J. D. Millerb, N. B. Drinnanc and W. Zmierczak, *Chem. Eng. J.*, 2011, **167**, 362–368.
44 F. Arena, G. Mezzatesta, G. Zafarana, G. Trunfio, F. Frusteri and L. Spadaro, *J. Catal.*, 2013, **300**, 141–151.
45 M. Maestri and K. Reuter, *Chem. Eng. Sci.*, 2012, **74**, 296–299.
46 H. Watanabe and M. Otaka, *Fuel*, 2006, **12–13**, 1935–1943.
47 M. A. Soria, C. Mateos-Pedrero, A. Guerrero-Ruiz and I. Rodrıguez-Ramos, *Int. J. Hydrogen Energy*, 2011, **36**, 15212–15220.
48 D. G. Avraam, T. I. Halkides, D. K. Liguras, O. A. Bereketidou and M. A. Goula, *Int. J. Hydrogen Energy*, 2010, **35**, 9818–9827.
49 S. Saeidi, N. A. S. Amin and M. R. Rahimpour, *J. CO_2 Util.*, 2014, **5**, 6–81.
50 M. Suk Lee, J. Y. Lee, D.-W. Lee, D. J. Moon and K. Y. Lee, *Int. J. Hydrogen Energy*, 2012, **37**, 11218–11226.
51 F. Malherbe, C. Forano, B. Sharma, M. P. Atkins and J. P. Besse, *Appl. Clay Sci.*, 1998, **13**, 381–399.
52 G. Pekridis, K. Kalimeri, N. Kaklidis, E. Vakouftsi, E. F. Iliopoulou, C. Athanasiou and G. E. Marnellos, *Catal. Today*, 2007, **127**, 337–346.